

Quantized Capacitance Charging of Monolayer-Protected Au Clusters

Shaowei Chen and Royce W. Murray*

Kenan Laboratories of Chemistry, University of North Carolina, Chapel Hill, North Carolina 27599-3290

Stephen W. Feldberg*

Department of Applied Sciences, Brookhaven National Laboratory, Upton, New York 11973-5000

Received: June 30, 1998; In Final Form: July 31, 1998

A theoretical model based on electrostatic interactions is developed to account for the formal potentials of current peaks observed in differential pulse voltammetry of solutions of 10 different nanometer-sized alkylthiolate and arylthiolate monolayer-protected gold clusters. The current peaks arise from successive, quantized (single-electron) capacitive charging of ensembles of individual cluster cores (i.e., electrochemical ensemble Coulomb staircase charging). Experimental peak potentials for a given cluster change roughly linearly with changes in its core charge state, as predicted by the theory, and the sub-attofarad capacitances (C_{CLU}) of individual clusters obtained from the slopes of such plots agree with those estimated from a simple concentric sphere capacitor model. The charging of clusters with very small cores becomes redox molecule-like, indicating as reported recently, the emergence of HOMO–LUMO energy gaps. Because the quantized charging currents of the clusters are diffusion controlled, their voltammetric behavior can be readily simulated, but requires attention to dispersities in C_{CLU} that occur in experimental samples of these materials. Simulations of microelectrode voltammetry incorporating Gaussian dispersions in cluster properties display features similar to those observed experimentally. The simulations show that quantized charging features are more difficult to detect when the nanoparticles are not monodisperse, but can be seen in polydisperse samples when the cores are small (small C_{CLU}) and not highly charged.

Introduction

An extensive research interest in nanometer-sized metal and semiconductor particles (“nanoparticles”) has arisen because of fundamental questions about this largely unexplored materials dimension and because of its diverse applications in optoelectronic devices, molecular catalysts, and chemical sensors.^{1,2} Despite extensive preparatory studies,² it has only recently become possible, starting with a report by Brust et al.,³ to isolate nanometer-sized metal (Au) clusters in solvent-free form that are stable and do not aggregate, can be redissolved without change, and can even be subjected to further synthetic manipulations.⁴ Stabilization of the Au (and subsequently described Ag,⁵ Pt,⁶ and alloy⁷) clusters is accomplished by protection by ligand monolayers of alkanethiolates and other thiolate ligands.^{8–10} The stability of these monolayer-protected clusters (MPCs) has made possible their solubility-based fractionation into monodisperse populations of nanoparticles.¹¹ Because of a combination of small metal-like core size and hydrocarbon-like dielectric coating, the capacitance (C_{CLU}) of an MPC can be less than an attofarad (aF) per MPC in (toluene/acetonitrile) electrolyte solutions. Addition or removal of single electrons from such tiny capacitors produces potential changes [$e/C_{\text{CLU}} \gg k_{\text{B}}T/e$], so that the solution phase, double-layer capacitance charging of the MPCs becomes a quantized property. This property of MPCs was demonstrated recently¹² and is an electrochemical analogue to Coulomb staircase charging.¹³ A further study has revealed a transition from metal-like double-layer capacitance charging to molecule-like redox charging as the MPC core size was decreased.¹⁴ We have since additionally observed quantized capacitance charging for arylthiolate-MPCs.¹⁵ Using differential

pulse voltammetry (DPV) to observe the quantized charging, data are now in hand for 10 cluster solutions which have displayed multiple-peak DPV responses.

Sequential electron transfers observed with fullerene (and derivatives)¹⁶ and Pt–carbonyl nanoclusters [$\text{Pt}_n(\text{CO})_m$]¹⁷ led Weaver et al.¹⁸ to develop an electrostatic model to relate the electron-transfer energetics of molecular capacitances in gas- and solution-phase systems. This paper uses this earlier theory to explain the charging energetics of Au MPCs and expands it to the diffusion-controlled voltammetry of monodisperse and polydisperse (in core size) Au MPCs. The Au MPCs differ from the fullerenes and Pt–carbonyl clusters in that they (a) display oxidative as well as reductive charging, (b) are somewhat larger and tend (except for the smallest examples¹⁴) to be metal-like, and (c) involve a monolayer shell the thickness and chemical dielectric characteristics of which can, in principle, be systematically varied.

The general conclusion drawn from the electrostatic theory in light of the available charging data is that the theory quite well represents the potentials of DPV peaks for successive, single-electron charging of MPCs. The “formal potentials” of the charging peaks are referenced to the potential of zero charge of the clusters (E_{PZC} , which is independently established). Exceptions to the predicted electrostatic behavior are seen for the smallest and most molecule-like of the MPCs, owing to the development of HOMO–LUMO gaps, and are manifested in large spacings between charging peaks immediately adjacent to the E_{PZC} . We also observe that since currents for kinetically rapid quantized charging steps are controlled by diffusion of the MPCs to the electrode,^{12,14} their voltammetry can be

described using the classical combination of Nernst and Fick's equations. We illustrate this using simulations of steady-state microelectrode voltammograms. The simulations also show that dispersity in the MPC capacitance causes gradual loss of quantized charging features in the voltammetry, just as observed experimentally.¹⁵

Theory

The theoretical approach to formulating the potentials at which successive single electron transfers arising from quantized charging of Au MPCs occur begins with simple electrostatic interactions, as described by Weaver et al.¹⁸ We extend his theory to point out the Nernstian behavior of such charging (assuming that the electron-transfer dynamics between the working electrode and MPCs are fast), to simulate the corresponding microelectrode voltammetry, and to account for effects of capacitance dispersity. Simplifications of the theory are (a) the MPC capacitance is based on an assumed spherical Au core (the actual core shape is postulated to be a truncated octahedron (TO)⁸ or truncated decahedron (TD)¹⁹), (b) effects of HOMO-LUMO gaps are neglected, and (c) the MPC capacitance is assumed to be independent of its state of charge.

Formal Potentials of Quantized Charging Reactions. This section describes the distribution of charges in a solution of monodisperse, spherical, metal-like nanoparticles (e.g., MPCs) in equilibrium with a working electrode. Of particular interest are the effects of successive single electron charging of the MPC, namely, the potentials at which these steps occur. The basic premise of the analysis is that the distribution of electrons between the working electrode and the MPCs is determined by the potential applied to the working electrode (E_{APP}), the potential of the MPC (E_P), and the (integral) capacitance (C_{CLU}) of an individual MPC:

$$E_P = E_{PZC} + \frac{ze}{C_{CLU}} \quad (1)$$

where E_{PZC} is the potential of zero charge of the nanoparticle, z is the number of electronic charges on the particle and is signed (i.e., if $z > 0$, the particle is oxidized while if $z < 0$, reduced), and e is the electronic charge (1.602×10^{-19} C).

The capacitance (C_{CLU}) of a spherical nanoparticle coated with a uniform monolayer (of dielectric constant ϵ) and in an electrolyte solution can be expressed as

$$C_{CLU} = A_{CLU} \frac{\epsilon\epsilon_0 r + d}{r} = 4\pi\epsilon\epsilon_0 \frac{r}{d}(r + d) \quad (2)$$

where E_0 is the permittivity of free space, A_{CLU} the surface area of the MPC core of radius r , and d the thickness of the protecting dielectric monolayer. Equation 2 predicts that when core size and protecting monolayer thickness are comparable (in the present study, $r = 0.5$ – 1.5 nm and $d = 0.5$ – 1.0 nm), C_{CLU} increases with increasing core radius, and for monolayers with similar dielectric property, decreases with increasing monolayer thickness. Considering the limits of eq 2, when $r \ll d$, $C_{CLU} = \epsilon\epsilon_0 A_{CLU}/r$, (e.g., a naked nanoparticle in a thick dielectric medium) and when $r \gg d$, $C_{CLU} = \epsilon\epsilon_0 A_{CLU}/d$ (akin to a monolayer on a flat surface).

The work W required to charge initially uncharged MPCs by z electrons to a potential E_P (see eq 1) with a working electrode

at potential E_{APP} is (at equilibrium)

$$W = \int_0^z e(E_{APP} - E_P) dz = ez \left[E_{APP} - \left(E_{PZC} + \frac{ze}{2C_{CLU}} \right) \right] \quad (3)$$

At the electrode/solution interface, the corresponding Boltzmann population (N_z) of MPCs having z charges relative to the population of uncharged MPCs (N_0) is

$$\frac{N_z}{N_0} = \exp\left(\frac{W}{k_B T}\right) = \exp\left\{ \frac{ze}{k_B T} \left[E_{APP} - \left(E_{PZC} + \frac{ze}{2C_{CLU}} \right) \right] \right\} \quad (4)$$

where k_B is the Boltzmann constant (1.38×10^{-23} J/K) and T is absolute temperature (K). The ratio (α_z) of the populations of adjacent charged states (differing by one electron in charge), N_z/N_{z-1} , is easily deduced from eq 4 as

$$\alpha_z = \frac{N_z}{N_{z-1}} = \exp\left\{ \frac{e}{k_B T} \left[E_{APP} - E_{PZC} - \frac{(z - 1/2)e}{C_{CLU}} \right] \right\} \quad (5)$$

An important observation at this point is that eq 5 is Nernstian in its form. Thus, a mixture of MPC particles having charge z and $z-1$ in a solution comprise, in a formal sense, a mixed valent solution of a "redox couple" with a formal potential, $E_{Z,Z-1}^o$, which is

$$E_{Z,Z-1}^o = E_{PZC} + \frac{(z - 1/2)e}{C_{CLU}} \quad (6)$$

The substance of this analogy of redox and nanoparticle behavior is that the latter can be *formally* regarded as a multivalent redox system which exhibits equally spaced formal potentials (assuming that C_{CLU} is independent of the charge state of the MPC).

A major difference, of course, between nanoparticles and conventional multivalent redox systems (such as $[Ru(bpy)_3]^{3+/2+/1+/0}$ where $bpy = 2,2'$ bipyridine), is that the electrochemical formal potentials of the latter are generally not evenly spaced for the first versus subsequent electron transfers, owing to molecular features of the complexes such as electronic coupling, ligand-metal or metal-metal interactions, and HOMO-LUMO gaps.²⁰ When such molecular effects are absent, that is, when C_{CLU} is independent of z , eq 5 predicts that the formal potentials of the capacitance charging steps should vary linearly with the valence states of the nanoparticle. From such plots one can evaluate the *average* nanoparticle capacitance. Additional information is required to identify the E_{PZC} and the adjacent charging steps for which $z = \pm 1/0$.

Core Size Distribution. Equation 2 shows that the capacitance C_{CLU} of the MPC depends on both core radius and protecting monolayer thickness. Experimentally, while the core shape cannot be accurately discerned, the core size can be evaluated by transmission electron microscopy (TEM). In addition, there is always some degree of dispersity of the observed core size, and therefore some dispersity of the cluster capacitance. Cluster samples as-prepared typically display some polydispersity, but repeated fractional recrystallization¹¹ can produce MPCs with a narrower size distribution and hence a more uniform value of C_{CLU} (i.e., approaching ideal monodispersity).

(It is worth observing that "dispersity" is not a simple concept and in fact requires consideration of variations in both core and monolayer. Also, experimental methods will not be equally sensitive to all forms of dispersity. That is, TEM and mass spectrometry detect core size dispersity. Electrochemical

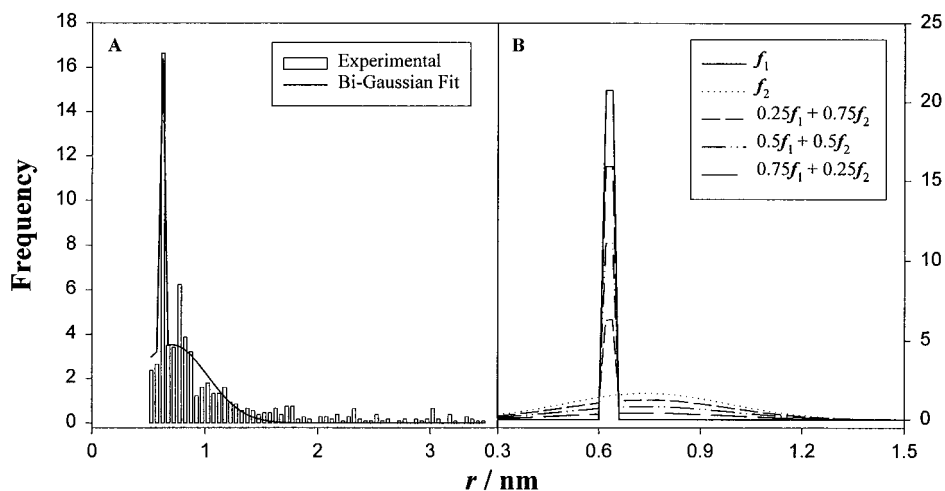


Figure 1. (A) TEM core size distribution (bar) of C4Au (28 kD) clusters and fit (—) with bi-Gaussian equation (eq 7b): $x_1 = 0.14$, $r_{01} = 0.63$ nm, $\sigma_1 = 0.01$ nm, $x_2 = 0.86$, $r_{02} = 0.74$ nm, $\sigma_2 = 0.34$ nm. (B) Computed bi-Gaussian core size distribution with varying compositions of two populations using the above r_0 and σ values (the maxima of the smaller core distributions have been truncated).

experiments detect dispersity in MPC capacitance, which can be determined by a combination of variation in the core size and packing in the monolayer shell, and by variations in the number of thiolate ligands attached to each MPC core. Fractional recrystallization separates MPCs on the basis of solubility dispersity, which is determined by a complex combination of all the monolayer structural and core size variations. In the present theory, we consider the dispersity in MPC capacitance as arising from variations on the core radius r . Considering dispersity alternatively as variations in the dielectric monolayer thickness d involves quite similar computations, which are not presented here.)

Clusters that have been fractionally recrystallized, and sometimes clusters that are crude synthetic products (i.e., arylthiolated Au MPCs¹⁵), give TEM images and core size distributions that can be approximated by a single

$$f(r) = \frac{1}{\sigma\sqrt{\pi}} \exp\left[-\frac{(r-r_0)^2}{\sigma^2}\right] \quad (7a)$$

or a bi-Gaussian function, i.e.,

$$f(r) = \frac{1}{\sqrt{\pi}} \left\{ \frac{x}{\sigma_1} \exp\left[-\frac{(r-r_{01})^2}{\sigma_1^2}\right] + \frac{1-x}{\sigma_2} \exp\left[-\frac{(r-r_{02})^2}{\sigma_2^2}\right] \right\} \quad (7b)$$

where r_0 is mean core radius and σ its standard deviation, subscripts 1 and 2 denote two populations with r_{01} and r_{02} mean core radii, and x is the mole fraction of the r_{01} population.

As an example, Figure 1A shows the TEM-derived core size distribution of a butanethiolate-protected Au MPC (abbreviated C4Au) that was partially fractionated and measured (by laser ionization/desorption mass spectrometry) to have a mean core mass of ca. 28 kD.¹⁴ The core size (r) distribution of this sample can be roughly represented by a bi-Gaussian function (eq 7b) in which 14% of the MPC population is narrowly centered at radius $r_{01} = 0.63$ nm (dispersity $\sigma_1 = 0.01$ nm) while a larger population (86%) is broadly distributed around radius $r_{02} = 0.74$ nm (dispersity $\sigma_2 = 0.34$ nm). Figure 1B illustrates how the core size dispersity would change with various proportions of the two different populations of r_{01} and r_{02} values and associated dispersities.

Electrochemical Responses. We have detected quantized charging of MPCs in solutions by several electrochemical techniques including pulse, cyclic, and steady-state microelectrode voltammetry.^{12,14,15} The voltammetric responses are diffusion controlled. Steady-state microelectrode voltammetry is the simplest of these techniques, and the derivative of the current–potential response should approximate the shape of differential pulse voltammograms (DPV, with which most of the quantized charging peak potentials have been measured). The limiting current for steady-state microelectrode voltammetry is

$$i = 4nr_{\text{EL}}FDC^* \quad (8)$$

where n is the number of electrons transferred, r_{EL} the microelectrode radius, F Faraday's constant, D the MPC diffusion coefficient, and C^* the MPC bulk concentration. The diffusion coefficient (D) is size-dependent and well approximated by the Einstein–Stokes equation

$$D = \frac{k_{\text{B}}T}{6\pi\eta r_{\text{H}}} \quad (9)$$

where η is solvent viscosity and r_{H} the hydrodynamic radius of the species. Results from rotating disk voltammetry²¹ suggest that MPC hydrodynamic radii can be roughly approximated by $r_{\text{H}} \approx r + d$. Combining eqs 7–9 gives the microelectrode current response as

$$i = 4nr_{\text{EL}}F \int_{r_{\text{LOW}}}^{r_{\text{HIGH}}} f(r) \left(\sum_{-N}^0 \frac{-1}{1 + \alpha_z} + \sum_1^N \frac{\alpha_z}{1 + \alpha_z} \right) \times \frac{k_{\text{B}}T}{6\pi\eta(r+d)} C^* dr \quad (10)$$

or

$$i_{\text{NORM}} = \int_{r_{\text{LOW}}}^{r_{\text{HIGH}}} f(r) \left(\sum_{-N}^0 \frac{-1}{1 + \alpha_z} + \sum_1^N \frac{\alpha_z}{1 + \alpha_z} \right) \frac{dr}{r+d} \quad (11)$$

where i_{NORM} is the normalized current [$i_{\text{NORM}} = (6i\pi\eta)/(4nr_{\text{EL}}FC^*k_{\text{B}}T)$] and r_{LOW} and r_{HIGH} are, respectively, the lower and upper limits of the core sizes (as observed experimentally). In eqs 10 and 11, the first and second summation terms within

TABLE 1: Formal Potentials of Quantized (Electrochemical Coulomb Staircase) Charging of Various Monolayer-Protected Au Nanoclusters^a

Au MPCs [core radius] (nm) ^b	$z/z-1^c$	$E_{P,C}$ (V) ^d	$E_{P,A}$ (V) ^d	E_P (V) ^d	ΔE_P (V) ^d	ΔV_C (V) ^d
C4Au (14 kD) [0.65]	+2/+1	0.530	0.582	0.556	0.052	
	+1/0	0.334	0.304	0.319	0.030	0.237
	0/-1	-0.410	-0.428	-0.419	0.018	0.738
	-1/-2	-0.714	-0.700	-0.707	0.014	0.288
C4Au (22 kD) [0.71]	+2/+1	0.438	0.483	0.461	0.045	
	+1/0	0.144	0.175	0.160	0.031	0.301
	0/-1	-0.255	-0.235	-0.245	0.020	0.405
	-1/-2	-0.604	-0.517	-0.561	0.087	0.316
C4Au (28 kD) [0.81]	-2/-3	-1.000	-0.947	-0.974	0.053	0.413
	+4/+3	0.714	0.709	0.712	0.005	
	+3/+2	0.550	0.520	0.535	0.030	0.177
	+2/+1	0.314	0.278	0.296	0.036	0.239
C6Au (8 kD) [0.55]	+1/0	0.010	-0.056	-0.023	0.066	0.319
	0/-1	-0.298	-0.332	-0.315	0.034	0.292
	-1/-2	-0.600	-0.632	-0.616	0.032	0.301
	+2/+1	0.670	0.820	0.745	0.150	
C6Au (22 kD) [0.71]	+1/0	0.370	0.490	0.430	0.120	0.315
	0/-1	-0.850	-0.740	-0.795	0.110	1.225
	-1/-2	-1.080	-0.920	-1.000	0.160	0.205
	+2/+1	0.270	0.330	0.300	0.060	
C6Au (28 kD) [0.81]	+1/0	-0.120	-0.060	-0.090	0.060	0.390
	0/-1	-0.420	-0.360	-0.390	0.060	0.300
	-1/-2	-0.760	-0.680	-0.720	0.080	0.330
	-2/-3	-1.000	-0.910	-0.955	0.090	0.235
C6Au (38 kD) [0.95]	+5/+4	0.933	0.894	0.914	0.039	
	+4/+3	0.717	0.736	0.727	0.019	0.187
	+3/+2	0.558	0.552	0.555	0.006	0.172
	+2/+1	0.308	0.288	0.298	0.020	0.257
PhC4SAu [1.05]	+1/0	-0.095	-0.096	-0.096	0.001	0.394
	0/-1	-0.376	-0.392	-0.384	0.016	0.288
	-1/-2	-0.688	-0.704	-0.696	0.016	0.312
	-2/-3	-1.031	-0.976	-1.004	0.055	0.308
PhC2SAu [1.06]	+5/+4	0.830	0.970	0.900	0.140	
	+4/+3	0.640	0.830	0.735	0.190	0.165
	+3/+2	0.430	0.580	0.505	0.150	0.230
	+2/+1	0.120	0.210	0.165	0.090	0.340
4-CresolSAu [1.50]	+1/0	-0.200	-0.076	-0.138	0.124	0.303
	0/-1	-0.430	-0.380	-0.405	0.050	0.267
	-1/-2	-0.690	-0.550	-0.620	0.140	0.215
	-2/-3	-0.850	-0.740	-0.795	0.110	0.175
PhC4SAu [1.05]	+3/+2	0.664	0.795	0.730	0.131	
	+2/+1	0.447	0.424	0.436	0.025	0.294
	+1/0	0.054	0.060	0.057	0.006	0.379
	0/-1	-0.180	-0.192	-0.186	0.012	0.243
PhC2SAu [1.06]	-1/-2	-0.394	-0.418	-0.406	0.024	0.220
	-2/-3	-0.926	-0.924	-0.925	0.002	0.519
	-3/-4	-1.310	-1.260	-1.285	0.050	0.360
	+7/+6	1.000	1.000	1.000	0	
4-CresolSAu [1.50]	+6/+5	0.800	0.900	0.850	0.100	0.150
	+5/+4	0.600	0.642	0.621	0.042	0.229
	+4/+3	0.458	0.483	0.471	0.025	0.150
	+3/+2	0.310	0.340	0.325	0.030	0.146
4-CresolSAu [1.50]	+2/+1	0.164	0.184	0.174	0.020	0.151
	+1/0	-0.012	0	-0.006	0.012	0.180
	0/-1	-0.206	-0.204	-0.205	0.002	0.199
	-1/-2	-0.383	-0.400	-0.392	0.017	0.187
4-CresolSAu [1.50]	-2/-3	-0.612	-0.512	-0.562	0.100	0.170
	+4/+3	0.462	0.400	0.431	0.062	
	+3/+2	0.242	0.216	0.229	0.026	0.202
	+2/+1	0.086	0.068	0.077	0.018	0.152
4-CresolSAu [1.50]	+1/0	-0.046	-0.088	-0.067	0.042	0.144

^a Peak positions were determined by differential pulse voltammetry (DPV) (experimental details in refs 14 and 15). While all were determined vs Ag/AgCl reference, differences in peak positions are experimentally much more certain than absolute potentials. ^b C4Au and C6Au denote butanethiolate and hexanethiolate MPCs, respectively; and PhC4SAu, 4-phenylbutyl-1-thiolate MPC; PhC2SAu, 2-phenylethylthiolate MPC; 4-CresolSAu, 4-thiolcresol MPC (these three arylthiolate MPCs were prepared at 0 °C and with 3-fold excess of thiol over Au) (ref 15); the core radii given for these MPCs are determined by TEM measurements (refs 10 and 15). ^c Valence state changes based on double-step chronocoulometric studies (ref 14), solution rest potentials (ca. -0.1 V), and impedance spectroscopic studies of nanoparticle monolayers on Au electrode surfaces where the potential of zero charge is ca. -0.2 V (ref 15). ^d Subscripts (A and C) denote anodic and cathodic peaks, $E_P = (E_{P,A} + E_{P,C})/2$, $\Delta E_P = E_{P,A} - E_{P,C}$, ΔV_C is the peak spacing between two adjacent peaks.

the parenthesis represent current contributions from adding electrons to or removing electrons from the MPC in the charging step, respectively. These equations can be used for numerical simulations and/or data fitting.

Simulations of cyclic voltammetry (CV) for macroelectrodes, where currents are not steady state, should be equally straightforward but are less valuable for comparison to experiment, since MPCs tend to physisorb from their solutions onto electrode surfaces with a coverage depending on the cluster concentration.²² In CV experiments, the resulting currents can be a combination of reactions of adsorbed and diffusing MPCs. Nonetheless, if the potentials for the successive charging steps are evident in the CV responses, they can be straightforwardly compared to the predictions of eqs 2 and 6.

Simulations and Discussion

In this section, the theory for MPC capacitance is compared to experimental values, followed by simulations of the steady-state microelectrode voltammetry of Au MPCs of different core sizes, protecting thiolate monolayers, and dispersity.

MPC Capacitances and Formal Potentials. Table 1 lists experimental results for differential pulse voltammetry (DPV) peak potentials, observed between -1 to $+1$ V vs Ag/AgCl for electrolyte solutions (mixed toluene/acetonitrile solvent) of 10 different Au MPCs (details of MPC nomenclature in Table 1 footnotes). Each peak potential represents a discernible charging step (above background). Experimental conditions and examples of DPV current–potential curves from which these data are derived have been previously presented.^{12,14} The small differences (ΔE_p) between DPV peak potentials in negative- and positive-going potential scans are mostly uncompensated iR effects. Small substructures (i.e., shoulders) occasionally seen in the DPV current–potential curves are ignored at this level of analysis. The parameter ΔV_C represents the difference between adjacent charging peaks. All of the alkanethiolate–MPC samples and the PhC4SAu sample in Table 1 had been fractionated; the other two arylthiolate–MPCs were unfractionated.

The assignment shown for the valence state change ($Z/Z-1$) for each peak in Table 1 is based on E_{PZC} having a value near -0.1 to -0.2 V (vs Ag/AgCl). This assignment was established by ac impedance measurements on a monolayer of C4Au (28 kD) MPCs attached to a Au electrode surface, that show a shallow double-layer capacitance minimum at ca. -0.2 V (vs Ag/AgCl)¹⁵ (i.e., a PZC around -0.2 V). This surface should be a good model for an MPC in solution. Additionally, rest potentials of naked Au electrodes in MPC solutions in this solvent are generally around -0.1 V. Thus, their reduction and oxidation processes occur at potentials more negative or positive than about -0.2 V, respectively.

Figure 2 compares the MPC formal potential (E_p) results from DPV to eq 6. Overall, the linearities of the changes of formal potential with valence state are excellent. (The exceptions to good linear fitting, the two smallest MPCs, 14 and 8 kD in Figures 2A and B, respectively, are discussed further below.) The overall Figure 2 result confirms our previous assertion¹⁴ that, for larger MPCs, the quantized capacitance charging steps can be regarded as double layer capacitance phenomena. The quantized capacitance charging in Table 1 and Figure 2 is analogous to Coulomb staircase charging of single nanoparticles, where equally spaced charging steps are predicted by theory and are experimentally seen.

The Figure 2 slopes and intercepts give corresponding MPC capacitances ($C_{CLU, EQN6}$) and E_{PZC} (eq 6), in Table 2. Table 2

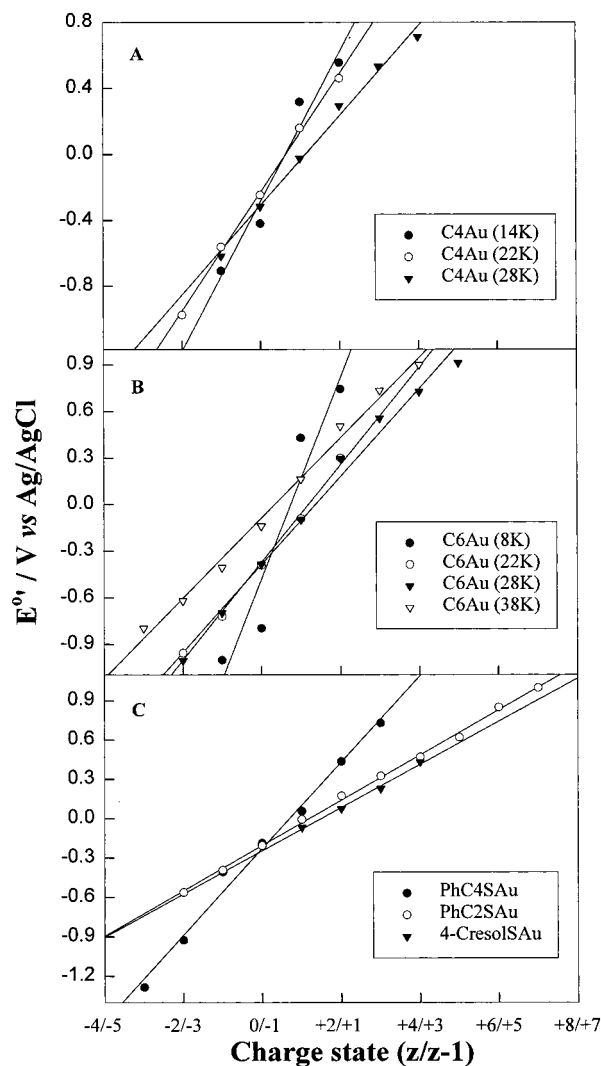


Figure 2. Formal potentials of the quantized capacitance charging of various Au MPCs versus their valence states where z refers to the couple $z/z-1$ (eq 6). Lines shown are linear regression.

TABLE 2: Formal Potentials of Quantized Capacitance Charging of Various Au Nanoparticles

Au MPCs	$C_{CLU,AV}$ (aF) ^a	$C_{CLU, EQN2}$ (aF) ^b	$C_{CLU, EQN6}$ (aF) ^c	E_{PZC} (V) ^c
C4Au (14kD)	0.22	0.49	0.35	-0.06
C4Au (22kD)	0.40	0.56	0.44	-0.05
C4Au (28kD)	0.50	0.69	0.59	-0.17
C6Au (8kD)	0.13	0.31	0.25	-0.16
C6Au (22kD)	0.41	0.45	0.51	-0.21
C6Au (28kD)	0.41	0.55	0.56	-0.24
C6Au (38kD)	0.53	0.71	0.62	-0.22
PhC4SAu	0.66	0.74	0.49	-0.06
PhC2SAu	0.89	1.22	0.93	-0.12
4-CresolSAu	1.11	2.79	0.97	-0.16

^a From quantized capacitance charging equation $C_{CLU,AV} = e/\Delta V_C$ where ΔV_C is the difference between peaks for $z = \pm 1/0$ [refs 12, 14, and 15]. ^b From eq 2: for C4 and C6 monolayers, $\epsilon = 3$, $d_{C4} = 0.52$ nm, and $d_{C6} = 0.77$ nm; for PhC4S monolayer $\epsilon = 3$, $d = 0.94$ nm, $r = 1.1$ nm; for PhC2S monolayer $\epsilon = 4$, $d = 0.67$ nm, $r = 1.1$ nm; for 4-CresolS monolayer $\epsilon = 5$, $d = 0.64$ nm, $r = 1.5$ nm; monolayer thicknesses (d) are approximated as fully extended chainlengths of the corresponding ligands (Hyperchem). ^c From plots of eq 6 (Figure 2).

also gives MPC capacitances ($C_{CLU,AV}$) derived (using the simple relation $V_C = e/C_{CLU,AV}$) from the spacings between DPV peaks that are adjacent to E_{PZC} (i.e., $z = \pm 1/0$). (The $C_{CLU,AV}$ results were reported previously¹⁴ for the alkanethiolate–MPCs.) Also

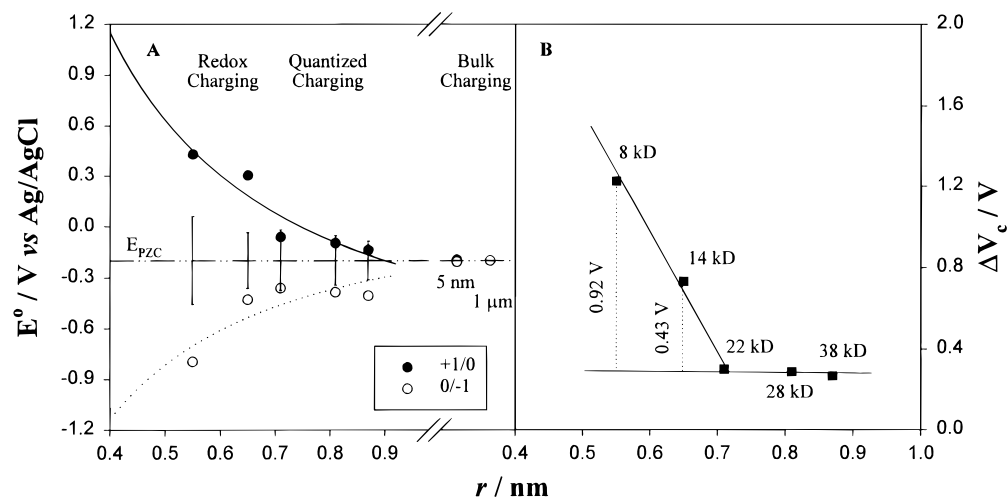


Figure 3. (A) Formal potentials of and (B) peak spacing between the $z = \pm 1/0$ peaks of C6:Au MPCs with various core sizes. (●) $z = +1/0$, and (○) $z = 0/-1$ (Data points of $r = 0.65$ nm are for C4Au MPC, 22 kD). The lines (—) and (···) are only guides to the eye. Vertical bars in part A are the theoretical predictions of ΔV_C for the C6:Au MPCs based on their $C_{CLU,EQN2}$ values in Table 2, centered around a supposed E_{PZC} of -0.2 V (— · — · —). The values of ΔV_C for illustrative larger particle dimensions (the “Bulk” domain) correspond to calculations from eq 2 using $\epsilon = 3$, $d_{C6} = 0.77$ nm, and $r = 5$ nm (a colloidal particle) and $r = 5 \mu m$ (a small microelectrode disk), giving 13 mV and $0.37 \mu V$, respectively.

given in Table 2 are capacitances $C_{CLU,EQN2}$ calculated from eq 2, using reasonable estimates of the relevant parameters (see table footnotes). Table 2 results for E_{PZC} lie between -0.05 and -0.22 V, which is consistent with how the $z = \pm 1/0$ valence state changes were assigned (vide supra). Variation of E_{PZC} values among the MPCs may reflect some structural properties, but equally likely, represent experimental uncertainty. It has been observed before for alkanethiol monolayers on flat surfaces²³ that E_{PZC} is difficult to determine.

Examination of Table 2 shows that MPC capacitances estimated from the spherical core model (eq 2, $C_{CLU,EQN2}$), agree reasonably well with those determined from plots of eq 6 ($C_{CLU,EQN6}$). The former tend to be somewhat larger than $C_{CLU,EQN6}$ values. On the whole, the spherical capacitor model of eq 2 works rather well. (Equation 2 produces a value for 4-CresolSAu MPCs that is much larger than the experimentally based capacitance. However, this MPC sample is unfractionated, and the core radius employed in the calculation (1.5 nm) is the average, TEM-derived value while the DPV peaks observed for this MPC are almost certainly dominated by the smaller nanoparticles in the distribution. The discrepancy thus reflects the less well-defined dimensions of the 4-CresolSAu MPCs.)

Further examination of Table 2 shows that, for MPCs with core mass ≥ 22 kD, reasonably good agreement is found between the average capacitances determined from Figure 2 ($C_{CLU,EQN6}$) and those ($C_{CLU,\Delta V}$) determined from the potential spacings between $z = 0/+1$ and $z = 0/-1$ chargings in DPV.^{12,14} For smaller MPCs (≤ 14 kD), the larger difference that appears between the capacitances is attributed to the fact that, at sufficiently small size, the clusters develop molecule-like redox behavior (i.e., a HOMO–LUMO gap as ascertained by comparison of their electrochemistry and spectroscopy).¹⁴ The redox property produces a larger potential spacing between the $z = +1/0$ and $z = 0/-1$ MPC valence changes, and thereby a $C_{CLU,\Delta V}$ capacitance that is smaller than that resulting from inclusion of charging peaks at more negative and positive potentials (according to eq 6, in the Figure 2 plots). Weaver et al.¹⁸ introduced an implicit quantum factor into his electrostatic relations, and the 8 and 14 kD MPCs of Table 2 are experimental examples which reflect such effects.

Figure 3 shows the effect of MPC core size on the charging potentials (part A) and the spacing between them (part B), for the $Z = +1/0$ and $0/-1$ peaks of C6Au MPCs. The $z = +1/0$ and $z = 0/-1$ peaks represent, formally, the solution analogues of ionization potential (IP) and electron affinity (EA), respectively.¹⁸ The enlarged spacing between the $z = +1/0$ and $z = 0/-1$ peaks for the two smallest core sizes in Figure 3 is consistent with the emergence of a HOMO–LUMO gap seen in near-IR spectroscopy of the clusters,¹⁴ and is greater than that anticipated with change in core radius from eq 2. The vertical bars in Figure 3A represent the predicted core radius dependency of ΔV_C (calculated from $C_{CLU,EQN2}$ in Table 2). Comparison of these theoretical predictions with the experimental points shows good agreement for MPCs with core radius ≈ 0.7 nm and mass ≥ 22 kD, but a substantial disagreement between the experimental E_p spacings and predictions of ΔV_C for the 8 and 14 kD core mass clusters. Figure 3B represents the changes in spacing in a way suggesting that the transition to more redox-like behavior¹⁴ begins at a cutoff core size of approximately 22 kD. (One would obviously like to see future additional experimental examples, on this important point of core size at which molecule-like properties start to occur.)

Finally, to illustrate a transition to the more conventional domain of double layer charging of larger gold particles, predictions of ΔV_C are shown at the right-hand side (large r) of Figure 3A for a small Au colloidal particle ($r = 5$ nm) and a small microelectrode. The predicted ΔV_C values for these larger sizes are below the range of current (room temperature) observability. According to the preceding discussion, the radius domains of Figure 3A are thus labeled (roughly) in terms of observing charging in “redox”, “quantized” (metal-like), and “bulk” (metal) size domains. Figure 3A thus shows that metal-like quantized capacitance charging can be expected to be observed only over a modest range of core dimensions.

The above evaluation is based on the cluster capacitances being independent of charge states (i.e., C_{CLU} is the same whether the MPC is positively or negatively charged). Some of the Table 1 data suggest that peaks are more closely spaced at extremes of positive and negative potentials, and it is well-known that double-layer capacitance varies with potential.²³ The Table 2 $C_{CLU,EQN6}$ results average such effects. The effect of the sign of the MPC charge state was examined by plotting

TABLE 3: Capacitance and Potential of Zero Charge of Various Monolayer-Protected Au Nanoclusters (MPCs) Determined from Plots of Equation 6 for Electrochemical Peaks at the Positive and Negative Valent States

Au MPCs	$C_{\text{CLU,EQN6}^+}$ (aF) ^a	$C_{\text{CLU,EQN6}^-}$ (aF) ^a	$E_{\text{PZC},+}$ (V) ^a	$E_{\text{PZC},-}$ (V) ^a	ΔE_{PZC} (V) ^b
C4Au (14kD)	0.67	0.56	0.20	-0.28	0.48
C4Au (22kD)	0.53	0.44	0.01	-0.05	0.06
C4Au (28kD)	0.65	0.53	-0.11	-0.17	0.06
C6Au (8kD)	0.51	0.78	0.27	-0.69	0.96
C6Au (22kD)	0.41	0.57	-0.29	-0.27	0.02
C6Au (28kD)	0.65	0.52	-0.13	-0.23	0.10
C6Au (38kD)	0.60	0.82	-0.23	-0.31	0.08
PhC4SAu	0.47	0.42	-0.10	0.06	0.04
PhC2SAu	0.96	0.90	-0.09	-0.12	0.03
4-CresolSAu	0.97		-0.16		

^a Subscripts (+ and -) denote states where $z > 0$ and $z \leq 0$, respectively. ^b (B) $\Delta E_{\text{PZC}} = |E_{\text{PZC},+} - E_{\text{PZC},-}|$.

data for the positive ($z > 0$) and negative ($z \leq 0$) valence states separately according to eq 6, again evaluating respectively (Table 3), values for $C_{\text{CLU,EQN6}^+}$ (from slope) and $C_{\text{CLU,EQN6}^-}$ and $E_{\text{PZC},+}$ and $E_{\text{PZC},-}$ (from intercepts). Overall, the $C_{\text{CLU,EQN6}^+}$ and $C_{\text{CLU,EQN6}^-}$ values for the various clusters are comparable and there seems to be no general bias that one is larger than the other. We conclude that the MPC capacitances are not very sensitive to the sign of their charge state (although surely they are not completely insensitive). The difference ΔE_{PZC} between $E_{\text{PZC},+}$ and $E_{\text{PZC},-}$ is more interesting. ΔE_{PZC} is less than 0.1V for the larger core size clusters but is large for the two smallest MPCs (e.g., ca. 0.97 V for C6Au (8 kD) and 0.48 V for C4Au (14 kD)). This is yet another manifestation of the onset¹⁴ of molecular-like redox properties for these materials.

Simulations of Microelectrode Voltammetry. The above analyses demonstrate that, except for those with very small cores, the charging energetics of MPCs are well represented by simple electrostatic relations. Simulations of microelectrode voltammetry were carried out with eq 11, with emphasis on the effects of core dimensions, core size dispersity and monolayer characteristics. Figure 4 shows simulated voltammetry for solutions of completely monodisperse clusters of varied core sizes but fixed monolayer thickness. It is readily evident that the charging steps are most easily observed for the smaller core clusters ($r < 1.25$ nm). Constant current step heights and step

spacings are observed because the MPC capacitance is assumed to be independent of electrode potential, and the peak spacing decreases with increasing core size since $\Delta V_c = e/C_{\text{CLU}}$ (as in classical Coulomb staircases¹³). For sufficiently large clusters, the responses gradually become ill-defined, as the peak spacings between the charging steps decrease. In the figure, this occurs at Au MPCs with a radius of (roughly) 1.25 nm, corresponding to ca. 586 Au atoms¹⁰ and a capacitance of ca. 1.4 aF (butanethiolate monolayer). Effects generally similar to those in Figure 4 can be expected by varying the monolayer thickness. Increasing monolayer thickness will increase the peak spacing and more clearly reveal the quantized charging features.

Experimentally, the Brust reaction⁴ does not yield monodisperse MPCs, but the core size dispersity can be reduced using repeated fractional recrystallization.¹¹ We believe that voltammetric quantized capacitance charging is likely to be very sensitive to dispersity, so it is worthwhile to model its effects. A simple case is a mixture of two monodisperse clusters of different core size. We chose MPCs with mean core radii equal to those in Figure 1A; the mean radii of these MPCs are not very different. Figure 5 shows the corresponding microelectrode voltammetry simulations for mixtures of the two monodisperse MPCs in various proportions, plus derivatives of the voltammograms, which are easier to visualize. Especially instructive is the (0.5 i_1 + 0.5 i_2) mixture where (- · · -) although the charging steps can be clearly seen near E_{PZC} , the different spacing between the peaks of the two populations dampens out the definition of the peaks at more negative and positive potentials.

A more realistic simulation assumes that an MPC has a Gaussian distribution of core sizes (eq 7a), this is shown in Figure 6. The figure assumes various levels of dispersity. For a radius dispersity (σ) that is about one-third of the mean radius, the peaks furthest removed from E_{PZC} are substantially lost. Even <10% dispersity ($\sigma < 0.1r_0$) has an effect on the peaks there. It is instructive, however, that even with extreme dispersity, the *central* pair of charging peaks remain visible in the derivative curve. This modeling says that the demands for monodispersity in observing quantized charging are most extreme when the MPCs are multiply charged, and least so when $z = \pm 1/0$.

A complex but more typical dispersity is multiple Gaussian distributions. Simulations (Figure 7) were made for the case

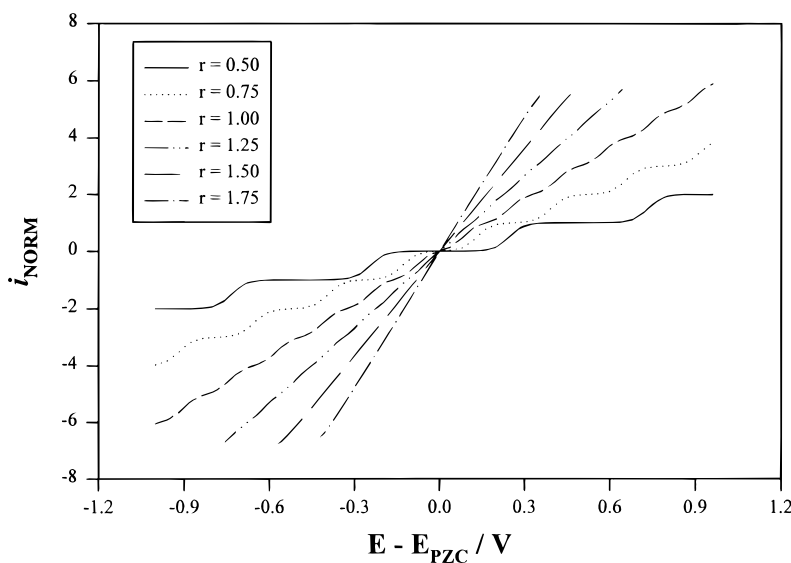


Figure 4. Steady-state microelectrode voltammetry simulations for completely monodisperse MPCs with various core sizes (r): $\epsilon = 3$, $T = 298\text{K}$, $d = 0.52$ nm, r values shown in nm.

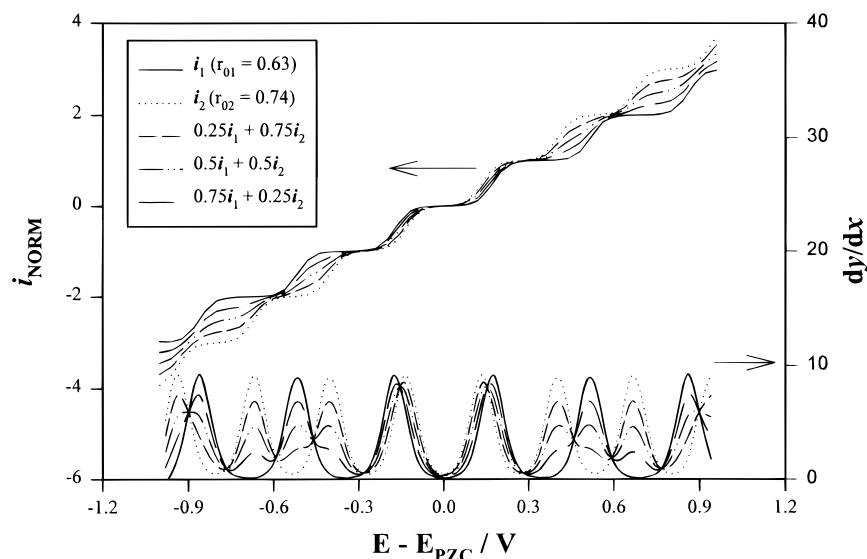


Figure 5. Steady-state microelectrode voltammograms simulations of a mixture of two monodisperse MPCs in various proportions as indicated by the multipliers of i_1 and i_2 : $\epsilon = 3$, $T = 298$ K, $r_{01} = 0.63$ nm, $r_{02} = 0.74$ nm, and $d = 0.52$ nm. Right-hand axis shows the first-order derivatives of the voltammograms.

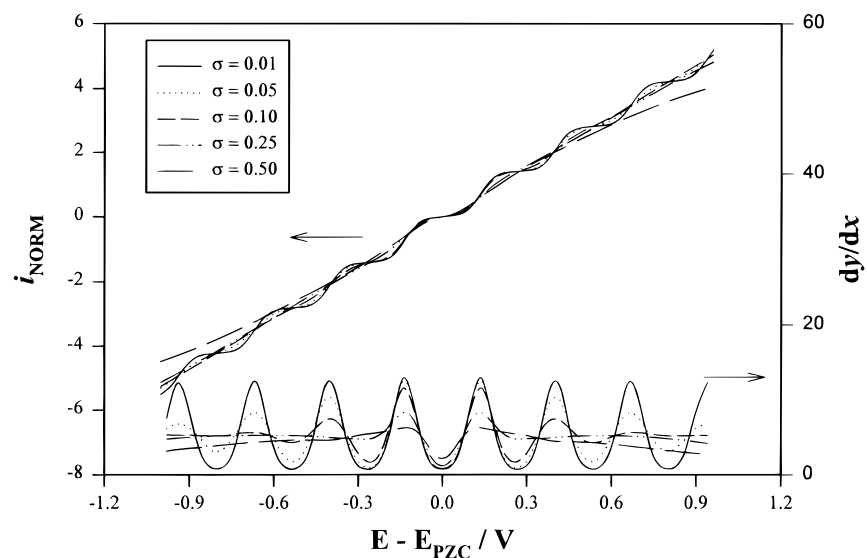


Figure 6. Steady-state microelectrode voltammograms simulations of MPCs with various core size dispersity: $\epsilon = 3$, $T = 298$ K, $r_0 = 0.74$ nm, $d = 0.52$ nm. σ values shown in nanometers. Right-hand axis shows the first-order derivatives of the voltammograms.

of the two populations (eq 7b) shown in Figure 1, (i.e., a small mean core size with a narrow distribution and a slightly larger core size with a much broader distribution). The results are analogous to those in Figures 5 and 6; with an increase in content of the more disperse component, the charging steps become less well-defined, and start to dampen out at potentials much more positive or negative than the PZC. The central spacing of peaks remains, however.

Finally, the simulations were applied to the actual experimental example of Figure 1 (a solution of butanethiolate (C4)-protected Au nanoclusters). Figure 8 compares the experimental microelectrode voltammogram and simulated (eq 10, bi-Gaussian function) microelectrode voltammogram for this example, which contains (14% of the smaller radius, narrower distribution component; and 84% of the larger radius, broader distribution component). Looking at the derivative in Figure 8, the agreement between the simulation and experimental results is rough but reasonable. The actual currents and the positions of the peaks are close to one another; the discrepancies at extreme potentials are probably due to the microelectrode background

current. The quantized charging features are roughly reproduced in the simulation, especially the current step positions nearest E_{PZC} (ca. -0.15 V). The peaks of the simulated voltammogram match the experimental data least well at extreme potentials, where the simulated peak spacings seem to be larger than the experimental values (see the derivative comparison). The latter effect is probably due to oversimplification in modeling the core size distribution and neglect of possible potential dependence of cluster capacitance.

Conclusions

The electrostatic charging theory of Weaver et al.¹⁸ accounts quite well for the energetics of successive single electron transfers of alkanethiolate and arylthiolate monolayer-protected Au clusters. The cluster capacitances are roughly independent of charge state, and experimental results are close to those calculated from a simple model of the clusters as concentric sphere capacitors. The model can be anticipated to be useful as a basis for evaluating cluster dimensions or to demonstrate expected electrochemical properties of new varieties of nano-

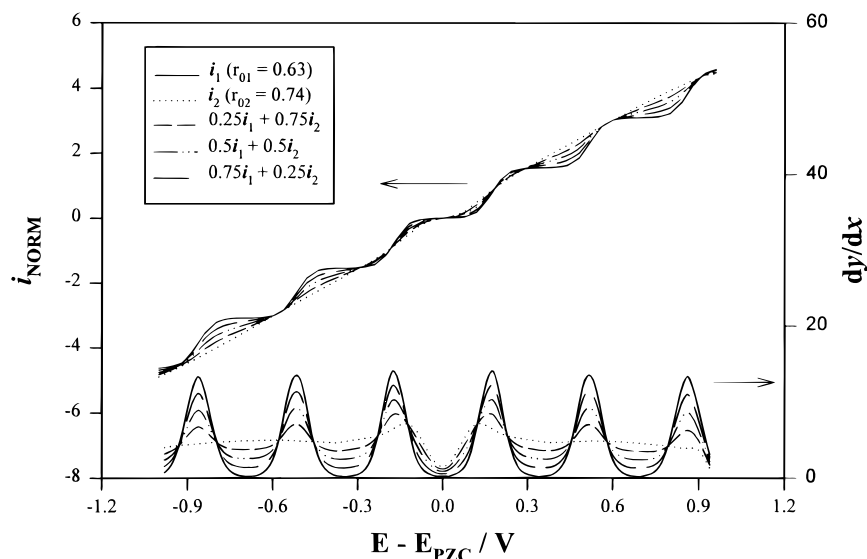


Figure 7. Steady-state microelectrode voltammograms simulations of a mixture of two MPCs with a Gaussian distribution of core radii in various proportions: $\epsilon = 3$, $T = 298\text{K}$, $d = 0.52\text{ nm}$, $r_{01} = 0.63\text{ nm}$, $\sigma_1 = 0.01\text{ nm}$, $r_{02} = 0.74\text{ nm}$, $\sigma_2 = 0.34\text{ nm}$. Right-hand axis shows the first-order derivatives of the voltammograms.

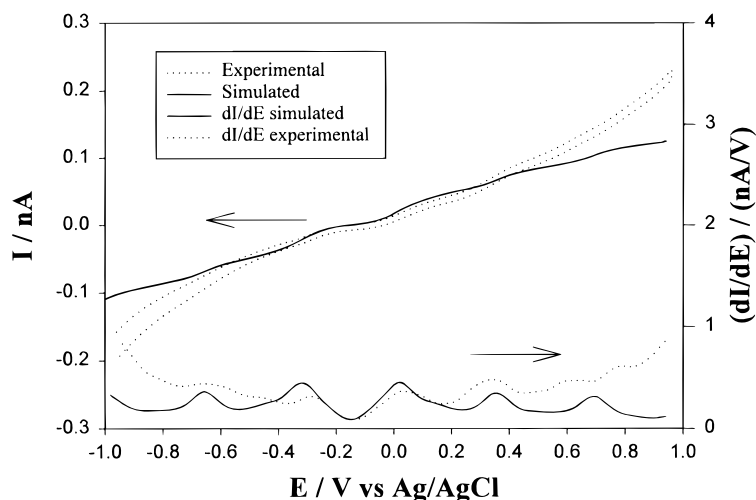


Figure 8. Experimental (dotted lines) and simulated (solid lines) microelectrode voltammograms for a butanethiolate-protected Au MPC solution: cluster concentration (C^*) = 0.10 mM, potential sweep rate 30 mV/s, electrode radius (r_{EL}) = 5 μm , supporting electrolyte 0.05 M tetra-*n*-hexylammonium perchlorate in a mixed solvent of toluene:acetonitrile (2:1 v:v) ($\eta = 0.50\text{ cP}$). Simulation is carried out with the parameters in Figure 1A in addition to $d = 0.52\text{ nm}$, $E_{\text{PZC}} = -0.15\text{ V}$, and $\epsilon = 3$. Right-hand axis shows the first-order derivatives of the voltammograms.

particles. Additionally, the model is not specific to any certain kind of core material, and thus can be used to evaluate electrostatic charging properties of nanoparticles based on different metals, on their alloys, and on other structural geometries. Importantly, the model has usefulness in detecting the onset of molecule-like redox properties, the most typical of which will be a larger and/or nonuniform spacing of charging peaks in the voltammetry of smaller nanoparticles.

Our previous studies^{12,14,15} of quantized capacitance chargings of monodisperse alkanethiolate Au clusters pointed out that the charging currents were determined by the rate of transport of the clusters through the solution to the working electrode surface. The electrochemical currents and those observed in the single-nanoparticle Coulomb staircase¹³ experiment are controlled by different factors. In the latter experiment, the cluster/contact capacitance determines both the current and the potential spacing between successive charging steps. In the electrochemical analogue, the cluster capacitance (in the electrostatic model) determines the spacing of successive single electron chargings.

The current is controlled by the mass transport properties of the cluster and of the electrochemical method used.

For such electrochemical currents for cluster charging reactions that are reversible and diffusion-controlled, Fick's relations and the Nernst equation can be employed to predict the cluster voltammetry. In this sense, the voltammetry of a monodisperse metal cluster is anticipated to be quite analogous to that of a redox molecule like ferrocene, except whereas ferrocene displays a single valence state change, the cluster should exhibit a series of roughly equally spaced voltammetric chargings at potentials *both* positive and negative of its potential of zero charge. If the single-electron cluster charging steps are slow (owing for example to the barrier posed by a long-chain protecting monolayer), then quasi-reversible voltammetric relations could be employed to analyze their behavior, again in analogy to redox species.

Another difference between cluster quantized charging voltammetry and redox molecule behavior is that clusters can exhibit a dispersion of capacitance owing to variations in core

size or some other dimensional characteristic. Electrochemical simulations show that quantized capacitance charging steps are most readily observed when the clusters have very small capacitances and small dispersities. An increase of capacitance dispersity causes the charging features to become less well-defined especially when an initially neutral cluster becomes charged multiple times.

Acknowledgment. This work was supported in part by grants from the National Science Foundation and the Office of Naval Research (S.C. and R.W.M.). S.W.F. gratefully acknowledges the support of the U.S. Department of Energy, Contract DE-AC02-98CH10886, and valuable comments from Marshall D. Newton (Brookshaven National Laboratory). The authors thank Professor R. L. Whetten and his students (Georgia Institute of Technology) for providing samples of the series of mono-disperse alkanethiolated MPCs. Some peak potentials in Table 1 were obtained and used in earlier joint publications.^{12,14}

References and Notes

- (1) For extensive reviews, see: (a) Hayat, M. A., Ed. *Colloidal Gold: Principles, Methods, and Applications*, Academic Press: San Diego, 1991. (b) Schmid, G., Ed. *Clusters and Colloids*; VCH: Weinheim, 1994. (c) *Proceedings of the Robert A. Welch Foundation 40th Conference on Chemical Research: Chemistry on the Nanoscale*; The Robert A. Welch Foundation: Houston, 1996.
- (2) (a) Schmid, G. *Chem. Rev.* **1992**, *92*, 1709. (b) Peschel, S.; Schmid, G. *Angew. Chem., Int. Ed. Engl.* **1995**, *34*, 1442. (c) Duteil, A.; Schmid, G. *J. Chem. Soc. Chem. Comm.* **1995**, 31. (d) Schmid, G.; Hess, H. *Z. Anorg. Allg. Chem.* **1995**, *621*, 147. (e) Petit, C.; Lixon, P.; Pileni, M. P. *J. Phys. Chem.* **1993**, *97*, 12974–12983. (f) Pileni, M. P. *Langmuir* **1997**, *13*, 3266–3276. (g) Sosebee, T.; Giersig, M.; Holzwarth, A.; Mulvaney, P. *Ber der Buns. Gesell. Phys. Chem.* **1995**, *99*, 40–49. (h) Lizmarzan, L. M.; Giersig, M.; Mulvaney, P. *Langmuir* **1996**, *12*, 4329–4335.
- (3) Brust, M.; Walker, M.; Bethell, D.; Schiffrin, D. J.; Whyman, R. *J. Chem. Soc. Chem. Comm.* **1994**, 801.
- (4) Templeton, A. C.; Hostetler, M. J.; Warmoth, E. K.; Chen, S.; Hartshorn, C. M.; Krishnamurthy, V. M.; Forbes, M. D. E.; Murray, R. W. *J. Am. Chem. Soc.* **1998**, *120*, 4845–4849.
- (5) Collier, C. P.; Saykally, R. J.; Shiang, J. J.; Henrichs, S. E.; Heath, J. R. *Science* **1997**, *277*, 1978–1981.
- (6) Sarathy, K. V.; Raina, G.; Yadav, R. T.; Kulkarni, G. U.; Rao, C. N. R. *J. Phys. Chem. B* **1997**, *101*, 9876–9880.
- (7) Hostetler, M. J.; Zhong, C.-J.; Yen, B. K. H.; Andereg, J.; Gross, S. M.; Evans, N. D.; Porter, M.; Murray, R. W. *J. Am. Chem. Soc.* In press.
- (8) Whetten, R. L.; Khoury, J. T.; Alvarez, M. M.; Murthy, S.; Vezmar, I.; Wang, Z. L.; Stephens, P. W.; Cleveland, C. L.; Luedtke, W. D.; Landman, U. *Adv. Mater.* **1996**, *8*, 428–433.
- (9) Hostetler, M. J.; Murray, R. W. *Curr. Opin. Colloid Interface Sci.* **1997**, *2*, 42–50.
- (10) Hostetler, M. J.; Wingate, J. E.; Zhong, C.-J.; Harris, J. E.; Vachet, R. W.; Clark, M. R.; Londono, J. D.; Green, S. J.; Stokes, J. J.; Wignall, G. D.; Glish, G. L.; Porter, M. D.; Evans, N. D.; Murray, R. W. *Langmuir* **1998**, *14*, 17–30.
- (11) Schaaff, T. G.; Shafiqullin, M. N.; Khoury, J. T.; Vezmar, I.; Whetten, R. L.; Cullen, W. G.; First, F. N.; Gutierrezwing, C.; Ascensio, J.; Joseyacamán, M. J. *J. Phys. Chem. B* **1997**, *101*, 7885–7891.
- (12) Ingram, R. S.; Hostetler, M. J.; Murray, R. W.; Schaaff, T. G.; Khoury, J. T.; Whetten, R. L.; Bigioni, T. P.; Guthrie, D. K.; First, P. N. *J. Am. Chem. Soc.* **1997**, *119*, 9279–9280.
- (13) (a) Hartman, E.; Marquardt, P.; Ditterich, J.; Radojkovic, P.; Steinberger, H. *Appl. Surf. Sci.* **1996**, *107*, 197. (b) Guo, L. Leobandung, E.; Chou, S. Y. *Science* **1997**, *275*, 649. (c) Amman, M.; Wilkins, R.; Ben-Jacob, E.; Maker, P. D.; Jaklevic, R. C. *Phys. Rev. B* **1991**, *43*, 1146. (d) Hofstetter, W.; Zwerger, W. *Phys. Rev. Lett.* **1997**, *78*, 3737.
- (14) Chen, S.; Ingram, R. S.; Hostetler, M. J.; Pietron, J. J.; Murray, R. W.; Schaaff, T. G.; Khoury, J. T.; Alvarez, M. M.; Whetten, R. L. *Science* **1998**, *280*, 2098.
- (15) Chen, S.; Murray, R. W. 1998. Submitted for publication.
- (16) (a) Haufler, R. E.; Conceicao, J.; Chibante, L. P. F.; Chai, Y.; Byrne, N. E.; Flanagan, S.; Haley, M. M.; O'Brien, S. C.; Pan, C.; Xiao, Z.; Billups, W. E.; Ciufolini, M. A.; Hauge, R. H.; Margrave, J. L.; Wilson, L. J.; Curl, R. F.; Smalley, R. E. *J. Phys. Chem.* **1990**, *94*, 8634–8636. (b) Li, Q.; Wudl, F.; Thilgen, C.; Whetten, R. L.; Diederich, F. *J. Am. Chem. Soc.* **1992**, *114*, 3994–3996.
- (17) Roth, J. D.; Lewis, G. J.; Safford, L. K.; Jiang, X.; Dahl, L. F.; Weaver, M. J. *J. Am. Chem. Soc.* **1992**, *114*, 6159.
- (18) Weaver, M. J.; Gao, X. *J. Phys. Chem.* **1993**, *97*, 332–338.
- (19) Cleveland, C. L.; Landman, U.; Schaaff, T. G.; Shafiqullin, M. N.; Stephens, P. W.; Whetten, R. L. *Phys. Rev. Lett.* **1997**, *79*, 1873–1876.
- (20) Ward, M. D. *Chem. Soc. Rev.* **1995**, *24*, 121–134.
- (21) Green, S. J.; Stokes, J. J.; Hostetler, M. J.; Pietron, J. J.; Murray, R. W. *J. Phys. Chem. B* **1997**, *101*, 2663.
- (22) Green, S. J.; Pietron, J. J.; Stokes, J. J.; Hostetler, M. J.; Vu, H.; Wuelfing, W. P.; Murray, R. W. *Langmuir*. In press.
- (23) Becka, A. M.; Miller, C. J. *J. Phys. Chem.* **1993**, *97*, 6233–6239.